

Fe²⁺-induced surface plasmon-catalyzed reduction reaction for the detection of Fe²⁺

Ye Sun

Liaoning University

Guangda Xu

Liaoning University

Yue Wang

Liaoning University

Peng song

Liaoning University

Yao Zhang (✉ zhangyao@lnu.edu.cn)

Liaoning University

Lixin Xia

Liaoning University

Research Article

Keywords: surface-enhanced Raman scattering spectroscopy, plasmon-catalyzed reduction reaction, Fe²⁺

Posted Date: May 13th, 2022

DOI: <https://doi.org/10.21203/rs.3.rs-1615696/v1>

License:  This work is licensed under a Creative Commons Attribution 4.0 International License.

[Read Full License](#)

Abstract

Herein, we developed a concise, time-efficient, and high selective assay for detecting Fe^{2+} through its triggered surface plasmon-catalyzed reduction reaction of *p*-nitrothiophenol (PNTTP) to *p,p'*-dimercaptoazobenzene (DMAB) based on surface-enhanced Raman scattering (SERS) spectroscopy. When Fe^{2+} was added to the PNTTP-AuNPs system, the appearance of three characteristic peaks at 1142, 1392, and 1140 cm^{-1} attributed to DMAB demonstrated that Fe^{2+} induced the catalytic coupling reaction of PNTTP. The Raman intensity ratio of the peak at 1142 cm^{-1} to the peak at 1336 cm^{-1} and the concentration of Fe^{2+} presented a good linear response from 10 to 100 μM with a limit of detection (LOD) of 0.35 μM . Besides, the probable reaction process has been put forward. More importantly, the entire detection process can be completed within 2 min and was used successfully for the detection of Fe^{2+} in river water.

1 Introduction

Iron is an indispensable trace element in the human body and participates in many physiological and pathological processes, such as oxygen transport[1], cell metabolism[2], enzyme exchange reactions[3], and electron transfer[4]. Excessive iron ions can cause cancer, Parkinson's disease and other diseases[5]; too few iron ions can produce various symptoms such as anaemia and syncope[6]. Thus, it is important to maintain an iron concentration within the normal range. The maximum allowable concentration in drinking water is 0.3 mg/L (about 5.4 μM) according to the World Health Organization recommendation[7]. As such, the detection and monitoring of iron is a topic of great significance. Traditional methods for detecting $\text{Fe}^{3+}/\text{Fe}^{2+}$ mainly include colourimetry[8, 9], fluorescence analysis[10–12], the electrochemical method[13–16], atomic absorption spectroscopy[17], and inductively coupled plasma mass spectrometry[18]. Although great progress has been made, these approaches still have some limitations, such as low sensitivity, complex preprocessing, and long detection time. Therefore, the development of a fast, concise, and inexpensive method is of great significance to human health and environmental monitoring.

In recent years, surface-enhanced Raman scattering (SERS) spectroscopy has been favoured by researchers due to its high sensitivity, non-destructive detection, fingerprint recognition ability, and short detection time[19, 20]. It has been widely applied in reaction mechanism monitoring[21], photocatalysis[22], medical diagnosis[23], and particularly in the field of trace analysis of various pollutants such as heavy metal ions[24], polycyclic aromatic hydrocarbons[25], pesticides[26], and bacteria[27]. For example, we proposed a label-free, fast, and highly sensitive assay for detecting Fe^{2+} using the surface-enhanced resonance Raman scattering (SERRS) technique with 2,2'-bipyridine as the probe[28]. Xu et al. prepared a two-dimensional Au@Ag nanorods array by the self-assembly method for the sensitive detection of thiram in apples[29]. Li's group used cetyltrimethylammonium bromide-induced aggregation of silver nanoparticles (AgNPs) to successfully detect hydroxylated polycyclic aromatic hydrocarbons in urine[30]. As typical examples of photo-induced plasmon-catalyzed reactions, the

conversion of *p*-aminothiophenol (PATP) and *p*-nitrothiophenol (PNTTP) to *p,p'*-dimercaptoazobenzene (DMAB) has attracted increasing attention, and a large number of related studies have been published[31, 32]. PATP and PNTTP can be converted into DMAB on AgNPs under laser induction, however, it is necessary to add extra oxidizing or reducing agents to achieve the similar conversion on gold nanoparticles (AuNPs). For instance, Liu et al. reported the catalytic coupling reaction of PATP to DMAB triggered by NO_2^- [33]. Further, Kneipp et al. found that Ag^+ , Au^{3+} , Pt^{4+} , and Hg^{2+} induced the conversion of PATP to DMAB[34]. However, there are few reports of the surface plasma reduction reaction from PNTTP to DMAB.

In this paper, we first proposed an Fe^{2+} -induced surface plasmon-catalyzed reduction reaction from PNTTP to DMAB for the determination of Fe^{2+} . Upon the addition of Fe^{2+} , the PNTTP-AuNPs system generated three new peaks at 1142, 1392, and 1140 cm^{-1} , indicating the formation of DMAB[35]. The designed SERS platform had a wide linear range from 10 to 100 μM with an LOD of 0.35 μM and excellent selectivity. More importantly, a possible reaction mechanism is described in this paper and the method was successfully applied to the detection of Fe^{2+} in river water, validating this new approach for the detection of Fe^{2+} .

2 Experimental

2.1 Materials

p-nitrothiophenol (PNTTP) was purchased from aladdin, Chloroauric Acid (HAuCl_4), sodium citrate, CaCl_2 , $\text{Co}(\text{NO}_3)_2 \cdot 6\text{H}_2\text{O}$, MgSO_4 , AgNO_3 , ZnCl_2 , KCl , $\text{H}_2\text{PtCl}_6 \cdot 6\text{H}_2\text{O}$, $\text{Pb}(\text{NO}_3)_2$, MnCl_2 , $\text{BaCl}_2 \cdot 2\text{H}_2\text{O}$, FeCl_3 , $\text{Cr}(\text{NO}_3)_3 \cdot 9\text{H}_2\text{O}$, $\text{Ni}(\text{NO}_3)_2 \cdot 6\text{H}_2\text{O}$, $\text{Cu}(\text{NO}_3)_2 \cdot 3\text{H}_2\text{O}$, NH_4Cl , $\text{FeSO}_4 \cdot 7\text{H}_2\text{O}$, H_2SO_4 were purchased from Sinopharm Chemical Reagent Co., LTD.

2.2 Apparatus

Scanning electron microscopic (SEM) characterization was used an FE-SEM Su-8010 system (Hitachi, Tokyo, Japan). Transmission electron microscopy (TEM) image was obtained by JEM-2100 ultra-high-resolution transmission electron microscope (JEOL, Japan). Ultraviolet–visible (UV–vis) spectroscopy was obtained a PerkinElmer Lambda 35 spectrophotometer (Norwalk, CT, USA). Inductive coupled plasma emission spectrometer (ICP-OES) test was performed on Optina 800 (PerkinElmer, USA). SERS spectra were recorded by a confocal Raman microspectrometer (Renishaw, UK) equipped with a $\times 50$ objective lens, under the excitation of a 633 nm laser.

2.3 Fabrication of AuNPs

The AuNPs were synthesized according to previous literature[36]. 1.5 mL sodium citrate (1% by weight) solution were injected quickly into the 250 mL round-bottom flask contained 100 mL boiling HAuCl_4 solution (0.01% by weight) and stirred magnetically for 20 min. Cooled the solution to room temperature and stored at 4 $^\circ\text{C}$ for the further use.

2.4 AuNPs modified with PNTP

Mixing 5 mL AuNPs and 5 mL PNTP (in ethanol) solution in a round flask and stirring at room temperature for 2 h. The prepared solution was stored at 4 °C for the next step.

2.5 SERS Measurement

The SERS spectra were taken from a Renishaw inVia Reflex confocal Raman system which the objective lens is 50× (NA = 0.75) and the diameter of the laser spot is 1 μm. The laser wavelength is 633 nm, the exposure time is 10 s and laser power is 17 mW. 100 μL AuNPs modified with PNTP were mixed with 100 μL Fe²⁺ or other cation solutions (100 μM) for 1 min, respectively. Afterward, The mixture was drawn into a capillary and tested.

2.6 Preparation of water samples

The river water was from the Hun river, Shenyang, Liaoning, China. The river water samples were filtered using 0.45 μm membrane and then were spiked with Fe²⁺ (20, 60 and 100 μM).

3 Results And Discussion

3.1 The characterization of AuNPs

We characterized the synthesized AuNPs by SEM, TEM and UV–vis absorption spectroscopy firstly. As can be seen in SEM and TEM photographs (Fig. 1A and Fig. 1B), AuNPs are spherical, uniform in size with a diameter of about 30 nm, and uniformly dispersed. The maximal UV–vis absorbance of AuNPs is at 526 nm (Fig. 1C), which is assigned to the surface plasma resonance of Au. The above characterization proved the successful synthesis of AuNPs.

3.2 The plasmon-catalyzed reduction reaction of PNTP to DMAB

Next, we measured the SERS spectrum of PNTP (Fig. 2a), and there was a typical peak at 1336 cm⁻¹ that is attributed to the vibration of the nitro group. When Fe²⁺ ions were added to the system, three new peaks appeared at 1142, 1392, and 1140 cm⁻¹ (Fig. 2c), suggesting that surface plasmon-catalyzed reduction reaction of PNTP to DMAB was triggered by Fe²⁺. Since H₂SO₄ solution was used in the process of preparation of the Fe²⁺ standard solution, the SERS spectrum of PNTP was tested in the presence of H₂SO₄ to exclude the influence of H₂SO₄. The result was present in Fig. 2b. When only H₂SO₄ solution was introduced into the PNTP-AuNPs system, it would not induce the conversion of PNTP to DMAB and even inhibited the combination of PNTP and AuNPs to a certain extent which is because of the significant decrease of the Raman intensity at 1336 cm⁻¹. The obtained results indicated that H₂SO₄ does not effect the PNTP-AuNPs-Fe²⁺ system.

According to previous reports[37], the PNTP-AgNPs system can be reduced to DMAB under the condition of irradiation. Therefore, we further explored whether the laser irradiation time can promote the conversion of PNTP to DMAB in the PNTP-AuNPs system. As shown in Fig. 3A, the characteristic peaks of PNTP hardly changed with the extension of illumination time from 10 to 60 s, suggesting that it is hard to convert PNTP to DMAB by laser illumination alone in this condition. Upon the addition of Fe^{2+} , the reduction process was completed quickly and accompanied by the appearance of new peaks. Figure 3B represented the Raman intensity ratios of the peaks at 1142 and 1392 cm^{-1} to the peak at 1336 cm^{-1} , defined as I_{1142}/I_{1336} and I_{1392}/I_{1336} (I represents the Raman intensity), which enhanced dramatically in the presence of Fe^{2+} . The above mentioned fully illustrated the important role of Fe^{2+} in the conversion from PNTP to DMAB, which could be considered as the theoretical basis for qualitative and semi-quantitative detection of Fe^{2+} .

3.3 Optimization of reaction condition

To obtain the best probe performance, we optimized necessary experimental conditions such as the concentration of PNTP and laser power. First, the final reaction concentration of PNTP was determined by fixing the Fe^{2+} concentration (100 μM) and changing the PNTP concentration. The experimental results are shown in Fig. S1. When the concentration of PNTP was 10^{-4} or 10^{-6} M, there were no characteristic peaks of DMAB generated. When the concentration was 10^{-3} M, the SERS intensity at 1141 cm^{-1} was weak. However, when the PNTP concentration was selected 10^{-5} M, there were obvious characteristic peaks at 1142, 1392 and 1440 cm^{-1} , which illustrated that PNTPs are more likely to undergo conversion to DMAB on AuNPs at this concentration (Fig. S1A). Therefore, the concentration of PNTP was determined to be 10^{-5} M in subsequent experiments. The laser power is also an important factor affecting the experimental results. The laser power is too weak to realize the Fe^{2+} -induced surface plasmon-catalyzed reduction reaction. Too strong power will cause the SERS intensity to exceed the range. It can be seen from Fig. S1B that the effect of converting PNTP to DMAB was the best with the laser power of 17 mW (100%), which was selected for the optimal laser power. higher than other cations, indicating the PNTP-AuNPs system has excellent selectivity towards Fe^{2+} .

3.4 Quantitatively SERS detection of Fe^{2+}

To explore the potential of SERS for quantitative detection of Fe^{2+} , we measured the SERS spectra of the PNTP-AuNPs system with the different concentration of Fe^{2+} (from 0 to 100 μM) and plotted the linear standard curves between the intensity ratio of I_{1142}/I_{1336} , I_{1392}/I_{1336} and Fe^{2+} concentration under the optimal conditions, which are presented in Fig. 4 and Fig. S2. With the increase of the concentration of Fe^{2+} , the SERS intensity at 1142 and 1392 cm^{-1} gradually increased (Fig. 4A). The SERS intensity ratio of I_{1142}/I_{1336} displayed a good linear relationship with Fe^{2+} concentration varying from 10 to 100 μM ($R^2 = 0.99248$) (Fig. 4B), while a worse value ($R^2 = 0.97367$) was obtained through the relationship between the SERS intensity ratio of I_{1392}/I_{1336} and the Fe^{2+} concentration (Fig. S2). Therefore, we chose the intensity ratio of I_{1142}/I_{1336} as the basis for quantitative detection of Fe^{2+} . In addition, the equation of the

regression line was $y = 0.14041 + 0.00586x$ (y represents the Raman intensity ratio of I_{1142}/I_{1336} and x represents the concentration of Fe^{2+}). The limit of detection (LOD) was calculated to be $0.35 \mu\text{M}$ according to $3\sigma/k$, where σ is the standard deviation of the background and k is the slope of the calibration curve.

3.5 Selectivity of the PNTP-AuNPs system

To further evaluate the specific selectivity of the system to Fe^{2+} , we examined the various environmentally relevant cations. Figure 5A exhibited the SERS responses of the PNTP-AuNPs system to Ca^{2+} , Au^{3+} , Co^{2+} , Mg^{2+} , Ag^+ , Zn^{2+} , K^+ , Pt^{4+} , Pb^{2+} , Mn^{2+} , Ba^{2+} , Fe^{3+} , Cr^{3+} , Ni^{2+} , Cu^{2+} , NH_4^+ and Fe^{2+} at the identical concentration. It was obvious that other cations cannot induce the formation of DMAB, only Fe^{2+} ions were able to trigger the surface plasmon-catalyzed reduction reaction of PNTP. Figure 5B intuitively revealed that the SERS intensity ratio of I_{1142}/I_{1336} , I_{1392}/I_{1336} for Fe^{2+} is significantly higher than other cations, indicating the PNTP-AuNPs system has excellent selectivity towards Fe^{2+} .

3.6 Practical application

Table 1

Determination of Fe^{2+} in practical samples via the proposed method and ICP-OES.

Samples	Spiked amount (μM)	SERS amount (μM)	SERS Recovery (%)	RSD (%) ($n = 6$)	Spiked Amount (μM)	ICP-OES Amount (μM)	ICP-OES Recovery(%)
River water	0	Not detected	–	–	0	Not detected	–
	20	16.13	80.65	4.27	20	20.30	101.50
	60	52.81	88.02	4.05	60	54.69	91.15
	100	102.72	102.72	3.77	100	91.66	91.66

To evaluate whether the proposed SERS platform could be used for actual sample detection, we selected river water for the spiked test. The SERS spectra of river water with different Fe^{2+} concentration was shown in Fig S3. It can be observed that the three new peaks of DMAB were generated when river water samples were spiked with Fe^{2+} (20, 60, and 100 μM), and the new peaks were absent without Fe^{2+} , which indicated that there was almost no Fe^{2+} in the river water samples. In addition, the comparison of the SERS method and ICP-OES is present in Table 1. Good recoveries ranged from 80.65–102.72% and a satisfactory relative standard deviation (RSD) was obtained, and the results were similar to ICP-OES method, which illustrated the proposed SERS sensor could be effectively applied to the detection of Fe^{2+} in river water. To further highlight the merit of this method, several strategies for detecting Fe^{2+} are presented in Table S2. It is obvious that the proposed SERS sensor had certain advantages in detection time, detection limit and linear range.

3.7 The possible reaction process

When the laser is irradiated on the AuNPs, pairs of "holes" and "electrons" are generated on the surface of the AuNPs[38]. With the addition of a reducing agent or oxidant, the corresponding "hole" or "electron" will be consumed, leading to the formation of isolated "electrons" or "holes", which causes the system to display reducibility or oxidizability. According to previous reports, we inferred the possible reaction process (Fig. 6). Specifically, the Fe^{2+} ions reacted with the oxidative "holes" generated on the surface of AuNPs and were oxidized to Fe^{3+} , so that a large number of isolated "electrons" existed which, in turn, reduced the two PNTP molecules to DMAB. Thus, the transformation of PNTP to DMAB can be expressed by the equation:



4 Conclusion

In conclusion, we reported a new strategy for the detection of Fe^{2+} by inducing surface plasmon reduction reaction of PNTP to DMAB based on SERS technology. The proposed method had a wide linear range from 10 to 100 μM with a LOD of 0.35 μM . The SERS platform had high selectivity to Fe^{2+} . In addition, the probable reaction mechanism was put forward. More importantly, the designed method had been successfully applied to detect Fe^{2+} in river water, which may achieve on-site detection of Fe^{2+} in the future.

Declarations

Funding

This work was supported by the National Natural Science Foundation of China (Grant No. 21671089), the Scientific Research Projects of Liaoning Provincial Department of Education (L2020002), the Liaoning Provincial Natural Science Foundation Joint Fund Project (2020-YKLH-22).

Competing Interests

The authors have no relevant financial or non-financial interests to disclose.

Author Contributions

All authors contributed to the study conception and design. Material preparation, data collection and analysis were performed by Ye Sun, Yue Wang, Peng Song, Yao Zhang and Lixin Xia. The first draft of the manuscript was written by Guangda Xu, Yao Zhang and Lixin Xia and all authors commented on previous versions of the manuscript. All authors read and approved the final manuscript.

Data Availability

All data generated or analysed during this study are included in this published article.

References

1. Zhu H, Peck SC, Bonnot F, Van Der Donk WA, Klinman JP (2015) Oxygen-18 kinetic isotope effects of nonheme iron enzymes HEPD and MPnS support iron (III) superoxide as the hydrogen abstraction species. *J Am Chem Soc* 137:10448–10451. <https://doi.org/10.1021/jacs.5b03907>
2. Chan SY, Zhang YY, Hemann C, Mahoney CE, Zweier JL, Loscalzo J (2009) MicroRNA-210 controls mitochondrial metabolism during hypoxia by repressing the iron-sulfur cluster assembly proteins ISCU1/2. *Cell Metab* 10:273–284. <https://doi.org/10.1016/j.cmet.2009.08.015>
3. Wen E, Yang X, Chen HB, Shaheen SM, Sarkar B, Xu S, Song H, Liang Y, Rinklebe J, Hou DY et al (2021) Iron-modified biochar and water management regime-induced changes in plant growth, enzyme activities, and phytoavailability of arsenic, cadmium and lead in a paddy soil. *J Hazard Mater* 407:124344. <https://doi.org/10.1016/j.jhazmat.2020.124344>
4. Jia R, Yang DQ, Xu DK, Gu TY (2018) Carbon steel biocorrosion at 80 °C by a thermophilic sulfate reducing archaeon biofilm provides evidence for its utilization of elemental iron as electron donor through extracellular electron transfer. *Corros Sci* 145:47–54. <https://doi.org/10.1016/j.corsci.2018.09.015>
5. Taalab YM, Ibrahim N, Maher A, Hassan M, Mohamed W, Moustafa AA, Salama M, Johar D, Bernstein L (2018) Mechanisms of disordered neurodegenerative function: concepts and facts about the different roles of the protein kinase RNA-like endoplasmic reticulum kinase (PERK). *Rev Neuroscience* 29: 387–415. <https://doi.org/10.1515/revneuro-2017-0071>
6. Cao XL, Bai YG, Li F, Liu FX, Lu SL (2019) One-pot synthesis of highly fluorescent poly (methacrylic acid)-capped silver nanoclusters for the specific detection of iron (II). *ChemistrySelect* 4:12183–12189. <https://doi.org/10.1002/slct.201903673>
7. Guan JP, Tu Q, Chen L, Yuan MS, Wang JY (2019) A benzothiazole-rhodol based luminophor: ES IPT-induced AIE and an application for detecting Fe²⁺ ion. *Spectrochim Acta Part A* 220:117114. <https://doi.org/10.1016/j.saa.2019.05.019>
8. Ondigo DA, Tshentu ZR, Torto N (2013) Electrospun nanofiber based colorimetric probe for rapid detection of Fe²⁺ in water. *Anal Chim Acta* 804:228–234. <https://doi.org/10.1016/j.aca.2013.09.051>
9. Ho TTT, Dang CH, Huynh TKC, Hoang TKD, Nguyen TD (2021) In situ synthesis of gold nanoparticles on novel nanocomposite lactose/alginate: recyclable catalysis and colorimetric detection of Fe (III). *Carbohydr Polym* 251: 116998. <https://doi.org/10.1016/j.carbpol.2020.116998>
10. Hirayama T, Tsuboi H, Niwa M, Miki A, Kadota S, Ikeshita Y, Okuda K, Nagasawa H (2017) A universal fluorogenic switch for Fe (II) ion based on N-oxide chemistry permits the visualization of intracellular redox equilibrium shift towards labile iron in hypoxic tumor cells. *Chem Sci* 8:4858–4866. <https://doi.org/10.1039/C6SC05457A>

11. Hirayama T, Inden M, Tsuboi H, Niwa M, Uchida Y, Naka Y, Hozumi I, Nagasawa H (2019) A Golgi-targeting fluorescent probe for labile Fe (II) to reveal an abnormal cellular iron distribution induced by dysfunction of VPS35. *Chem Sci* 10:1514–1521. <https://doi.org/10.1039/C8SC04386H>
12. Zhang DD, Tian XT, Li HH, Zhao YP, Chen L (2021) Novel fluorescent hydrogel for the adsorption and detection of Fe (III). *Colloid Surface A* 608:125563. <https://doi.org/10.1016/j.colsurfa.2020.125563>
13. Zhu Y, Pan DW, Hu XP, Han HT, Lin MY, Wang CC (2017) An electrochemical sensor based on reduced graphene oxide/gold nanoparticles modified electrode for determination of iron in coastal waters. *Sensor Actuat B Chem* 243:1–7. <https://doi.org/10.1016/j.snb.2016.11.108>
14. Rana S, Mittal SK, Kaur N, Banks CE (2017) Disposable screen printed electrode modified with imine receptor having a wedge bridge for selective detection of Fe (II) in aqueous medium. *Sensor Actuat B Chem* 249:467–477. <https://doi.org/10.1016/j.snb.2017.04.135>
15. Ma S, Pan DW, Wei H, Wang N, Pan F, Kang Q (2019) In-situ fabrication of reduced graphene oxide/leucomethylene blue/platinum nanoparticles modified electrode for voltammetric determination of trace Fe (II) in seawater. *Microchem J* 151:104210. <https://doi.org/10.1016/j.microc.2019.104210>
16. Nguyen LD, Huynh TM, Nguyen TSV, Le DN, Baptist R, Doan TCD, Dang CM (2020) Nafion/platinum modified electrode-on-chip for the electrochemical detection of trace iron in natural water. *J Electroanal Chem* 873:114396. <https://doi.org/10.1016/j.jelechem.2020.114396>
17. Ohashi A, Ito H, Kanai C, Imura H, Ohashi K (2005) Cloud point extraction of iron (III) and vanadium (V) using 8-quinolinol derivatives and Triton X-100 and determination of 10^{-7} mol dm⁻³ level iron (III) in riverine water reference by a graphite furnace atomic absorption spectroscopy. *Talanta* 65:525–530. <https://doi.org/10.1016/j.talanta.2004.07.018>
18. Su CK, Chen YT, Sun YC (2019) Speciation of trace iron in environmental water using 3D-printed minicolumns coupled with inductively coupled plasma mass spectrometry. *Microchem J* 146:835–841. <https://doi.org/10.1016/j.microc.2019.02.015>
19. Sun YD, Shi L, Mi L, Guo RY, Li T (2020) Recent progress of SERS optical nanosensors for miRNA analysis. *J Mater Chem B* 8:5178–5183. <https://doi.org/10.1039/D0TB00280A>
20. McNay G, Eustace D, Smith WE, Faulds K, Graham D (2011) Surface-enhanced Raman scattering (SERS) and surface-enhanced resonance Raman scattering (SERRS): a review of applications. *Appl Spectrosc* 65:825–837. <https://doi.org/10.1366/11-06365>
21. Zhang X, Wang PJ, Sheng SX, Zhang LS, Fang Y (2014) Direct visual evidence for chemical mechanism of SERRS of the S-complex of pyrimidine molecule adsorbed on silver nanoparticle via charge transfer. *Spectrochim Acta A* 121:430–435. <https://doi.org/10.1016/j.saa.2013.11.003>
22. Yan XF, Xu Y, Tian BZ, Lei JY, Zhang JH, Wang LZ (2018) Operando SERS self-monitoring photocatalytic oxidation of aminophenol on TiO₂ semiconductor. *Appl Catal B-Environ* 224:305–309. <https://doi.org/10.1016/j.apcatb.2017.10.009>
23. Rong Z, Wang CW, Wang JF, Wang DG, Xiao R, Wang SQ (2016) Magnetic immunoassay for cancer biomarker detection based on surface-enhanced resonance Raman scattering from coupled

- plasmonic nanostructures. *Biosens Bioelectron* 84:15–21.
<https://doi.org/10.1016/j.bios.2016.04.006>
24. Zhang XG, Dai ZG, Si SY, Zhang XL, Wu W, Deng HB, Wang FB, Xiao XH, Jiang CZ (2017) Ultrasensitive SERS substrate integrated with uniform subnanometer scale “hot spots” created by a graphene spacer for the detection of mercury ions. *Small* 13:1603347.
<https://doi.org/10.1002/smll.201603347>
25. Li D, Cao XK, Zhang QM, Ren XG, Jiang L, Li DW, Deng W, Liu HT (2019) Facile in situ synthesis of core–shell MOF@Ag nanoparticle composites on screen-printed electrodes for ultrasensitive SERS detection of polycyclic aromatic hydrocarbons. *J Mater Chem A* 7:14108–14117.
<https://doi.org/10.1039/C9TA03690C>
26. Xu Y, Kutsanedzie FY, Hassan M, Zhu JJ, Ahmad W, Li H, Chen QS (2020) Mesoporous silica supported orderly-spaced gold nanoparticles SERS-based sensor for pesticides detection in food. *Food Chem* 315:126300. <https://doi.org/10.1016/j.foodchem.2020.126300>
27. Pang YF, Wan N, Shi LL, Wang CW, Sun ZW, Xiao R, Wang SQ (2019) Dual-recognition surface-enhanced Raman scattering (SERS) biosensor for pathogenic bacteria detection by using vancomycin-SERS tags and aptamer-Fe₃O₄@ Au. *Anal Chim Acta* 1077:288–296.
<https://doi.org/10.1016/j.aca.2019.05.059>
28. Xu GD, Li N, Sun Y, Gao C, Ma LP, Song P, Xia LX (2021) A label-free, rapid, sensitive and selective technique for detection of Fe²⁺ using SERRS with 2, 2'-bipyridine as a probe. *Chem Eng J* 414:128741. <https://doi.org/10.1016/j.cej.2021.128741>
29. Pu HB, Huang ZB, Xu F, Sun DW (2021) Two-dimensional self-assembled Au-Ag core-shell nanorods nanoarray for sensitive detection of thiram in apple using surface-enhanced Raman spectroscopy. *Food Chem* 343:128548. <https://doi.org/10.1016/j.foodchem.2020.128548>
30. Gao Y, Li LF, Zhang X, Wang XN, Ji W, Zhao JZ, Ozaki Y (2019) CTAB-triggered Ag aggregates for reproducible SERS analysis of urinary polycyclic aromatic hydrocarbon metabolites. *Chem Commun* 55:2146–2149. <https://doi.org/10.1039/C8CC09008D>
31. Chu JY, Miao P, Han XJ, Du YC, Wang XJ, Song B, Xu P (2016) Ultrafast surface-plasmon-induced photodimerization of p-Aminothiophenol on Ag/TiO₂ nanoarrays. *ChemCatChem*. 8:1819–1824.
<https://doi.org/10.1002/cctc.201600172>
32. Xia LX, Ma CQ, Wang J, Wu SW, Liu Y, Zhang Q, Song P (2017) A new strategy for effective distance regulation of the surface plasmon assisted coupling reaction of p-nitrothiophenol to p, p'-dimercaptoazobenzene. *Chem Commun* 53:9582–9585. DOI <https://doi.org/10.1039/C7CC04780K>
33. Liu XJ, Tang LH, Niessner R, Ying YB, Haisch C (2015) Nitrite-triggered surface plasmon-assisted catalytic conversion of p-aminothiophenol to p, p'-dimercaptoazobenzene on gold nanoparticle: surface-enhanced Raman scattering investigation and potential for nitrite detection. *Anal Chem* 87:499–506. <https://doi.org/10.1021/ac5039576>
34. Zhang ZG, Merk V, Hermanns A, Unger WE, Kneipp J (2017) Role of metal cations in plasmon-catalyzed oxidation: a case study of p-aminothiophenol dimerization. *ACS Catal* 7:7803–7809.

<https://doi.org/10.1021/acscatal.7b02700>

35. Liang X, You TT, Liu DP, Lang XF, Tan EZ, Shi JH, Yin PG, Guo L (2015) Direct observation of enhanced plasmon-driven catalytic reaction activity of Au nanoparticles supported on reduced graphene oxides by SERS. *Phys Chem Chem Phys* 17:10176–10181. <https://doi.org/10.1039/C5CP00908A>
36. Lu DC, Lin XL, Chen CR, Lu YD, Feng SY, Huang ZF, You RY, Chen JB, Wu Y. (2020) Interference-free SERS tags for ultrasensitive quantitative detection of tyrosinase in human serum based on magnetic bead separation. *Anal Chim Acta* 1138:150–157. <https://doi.org/10.1016/j.aca.2020.09.042>
37. Kang LL, Xu P, Zhang B, Tsai H, Han XJ, Wang HL (2013) Laser wavelength- and power-dependent plasmon-driven chemical reactions monitored using single particle surface enhanced Raman spectroscopy. *Chem Commun* 49:3389–3391. <https://doi.org/10.1039/C3CC40732B>
38. Yan XF, Wang LZ, Tan XJ, Tian BZ, Zhang JL (2016) Surface-enhanced Raman spectroscopy assisted by radical capturer for tracking of plasmon-driven redox reaction. *Sci Rep* 6:1–7. <https://doi.org/10.1038/srep30193>

Figures

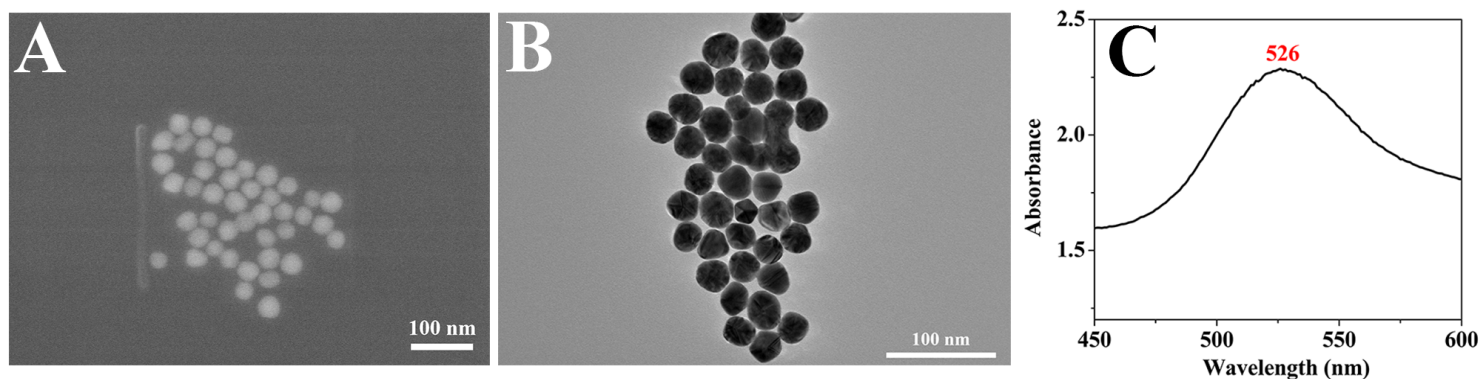


Figure 1

(A) SEM image of AuNPs. (B) TEM image of AuNPs. (C) UV-vis spectrum of AuNPs.

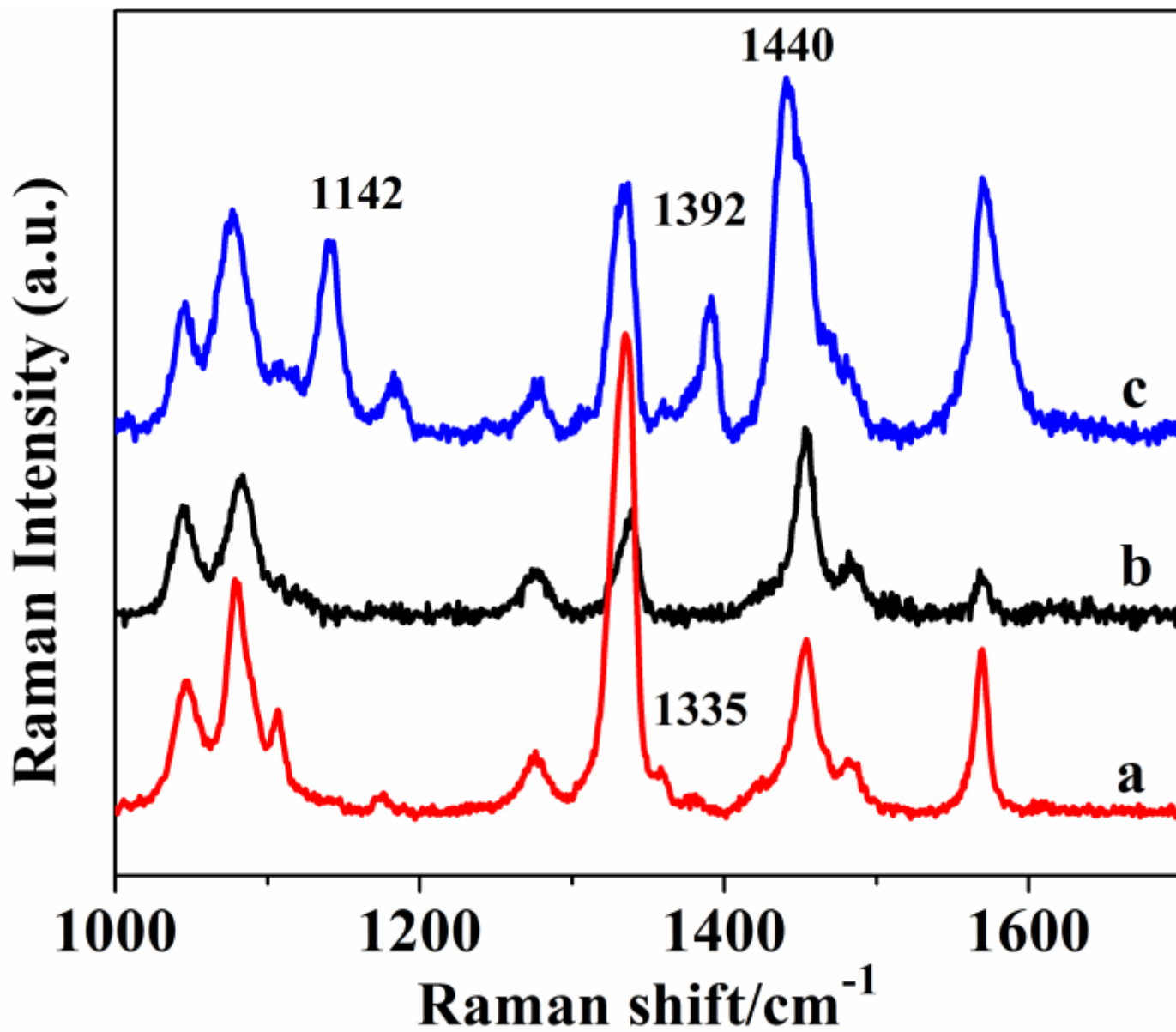


Figure 2

(a) SERS spectrum of PNTP. (b) SERS spectrum of PNTP in the presence of H₂SO₄. (c) SERS spectrum of PNTP in the presence of Fe²⁺ (100 μM).

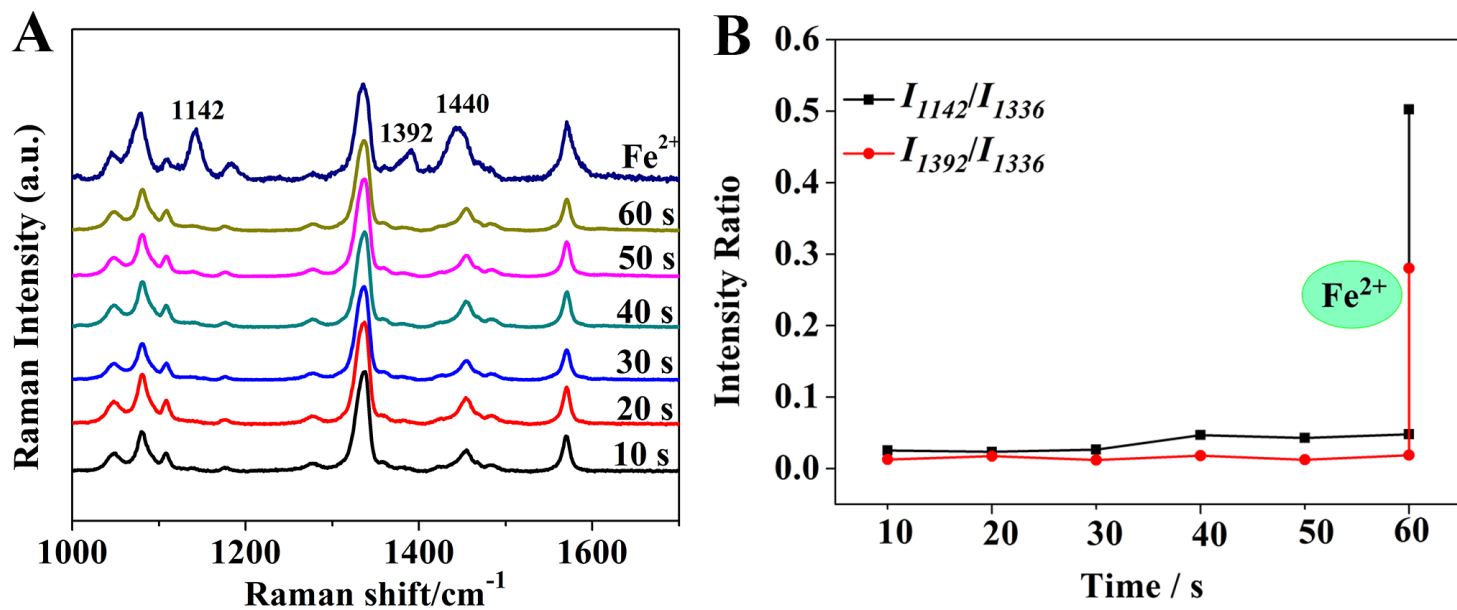


Figure 3

(A) SERS spectra of the effect of different time and Fe²⁺ on the PNTF-AuNPs system. (B) The line chart of the effect of different time and Fe²⁺ on the PNTF-AuNPs system.

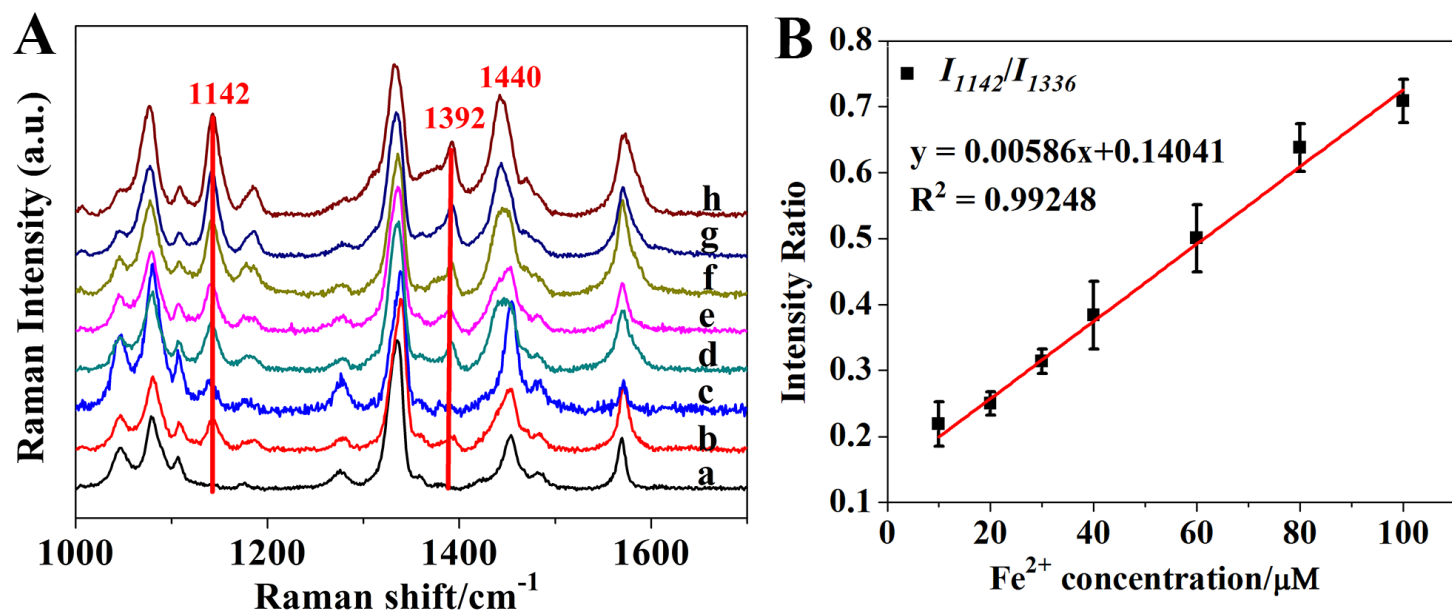


Figure 4

(A) SERS spectra of the PNTF-AuNPs system with the different concentration of Fe²⁺. (B) The linear plot of the intensity ratio against different Fe²⁺ concentrations. The error bars represent three independent experiments.

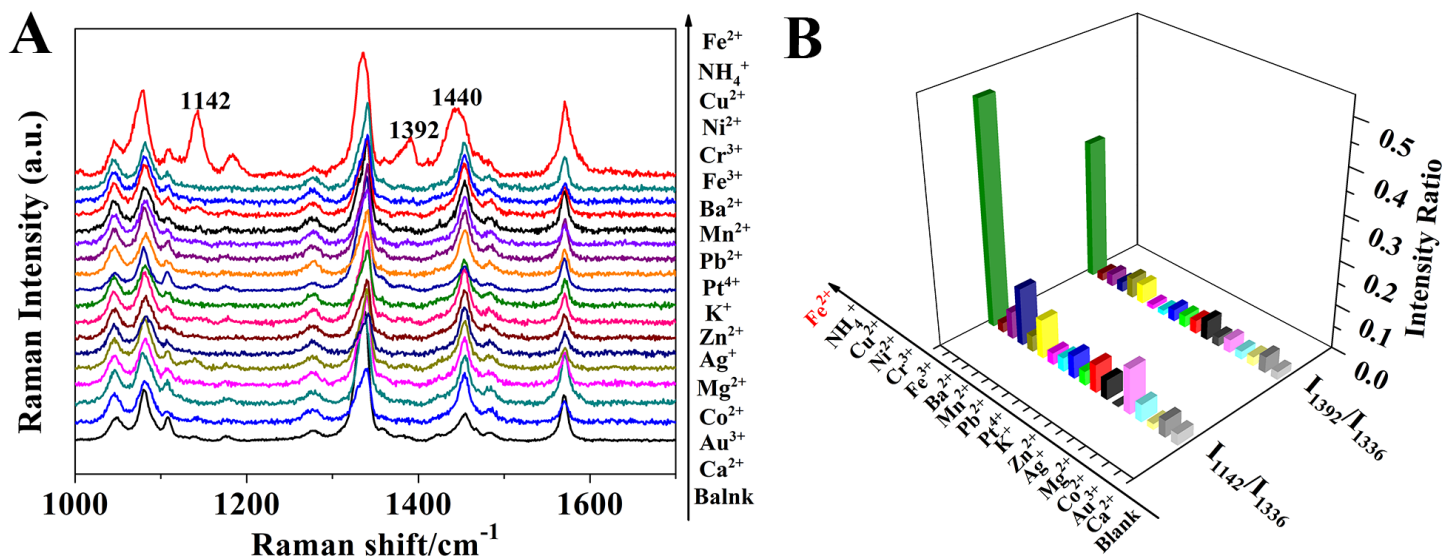


Figure 5

(A) Specificity test with the same concentrations of various cations. (B) The three-dimensional histogram of the intensity ratio of I_{1142}/I_{1336} , I_{1392}/I_{1336} with different cations.

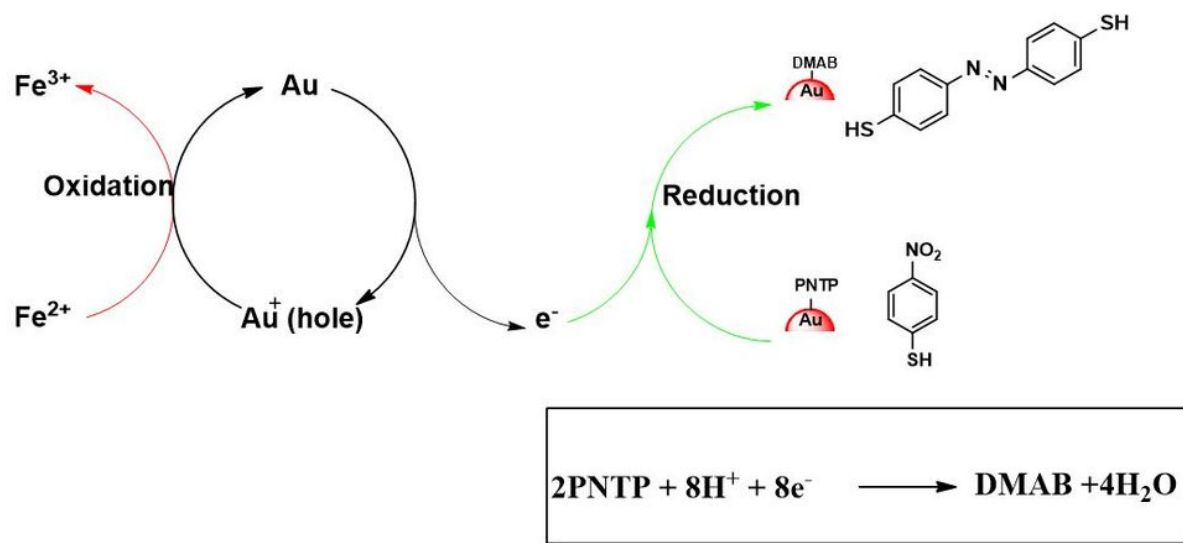


Figure 6

Schematic diagram of conversion mechanism of PNTTP to DMAB in PNTTP-AuNPs-Fe²⁺ system.

Supplementary Files

This is a list of supplementary files associated with this preprint. Click to download.

- [Sl.docx](#)